$La_{0.5}Ba_{0.5}Cu_xFe_{1-x}O_{3-\delta}$ as cathode for high-performance proton-conducting solid oxide fuel cell

Shenglin Liu [a], Menglin, Wu [a], Lanying Lu [b], Jiupai Ni [a,c], Chengsheng Ni [a,c], John T.S. Irvine [a,d*]*

a College of Resources & Environment, Southwest University, Chongqing 400715, China

b Chongqing Technology and Business University, Nan'an district, Chongqing, 400067 China

c National Base of International S&T Collaboration on Water Environmental Monitoring and Simulation in Three Gorges Reservoir Region, Chongqing 400716, China

d School of Chemistry, University of St Andrews, Fife, UK, KY16 9ST.

Corresponding author: C.N. nichengsheg@swu.edu.cn; J.T.S.I. jtsi@st-andrews.ac.uk

Abstract:

$La_{0.5}Ba_{0.5}Cu_xFe_{1-x}O_{3-\delta}$ ($0 \le x \le 1$) perovskite was investigated as a cathode for a protonic solid oxide fuel cell (H-SOFC) using $BaZr_{0.1}Ce_{0.7}Y_{0.2}O_{\delta}$ (BZCY) electrolyte. A maximum electric conductivity (76.84 S cm^{-1} at 700 ^oC) was achieved in the air at the composition of $La_{0.5}Ba_{0.5}Cu_{0.4}Fe_{0.6}O_{3-\delta}$. Comparing to $La_{0.5}Ba_{0.5}CuO_{3-\delta}$ (LBC), the increase in Fe content increased the D_{chem} ($1.07x10^{-5}$ to $1.74x10^{-5}$ cm^2 S^{-1}) and K_{chem} ($1.12x10^{-10}$ to $3.01x10^{-10}$ cm^2 S^{-1}) at $La_{0.5}Ba_{0.5}Cu_{0.2}Fe_{0.8}O_{3-\delta}$ (LBCF28) but decreased the proton conductivity from 7.5 to 4.3 mS cm^{-1}. Either Fe doping in LBC or Cu doping in $La_{0.5}Ba_{0.5}FeO_{3-\delta}$ increased the thermal expansion coefficient (TEC), but a low TEC among samples with mixed cations was achieved at $La_{0.5}Ba_{0.5}Cu_{0.5}Fe_{0.5}O_{3-\delta}$ (LBCF55) (16.12 ppm K^{-1}). LBC suffered from superficial decomposition in the ambient air, causing an ohmic resistance loss of the full cell on Ni(O)-BZCY support. A high initial cell performance (820 mW cm^{-2}) can be achieved for the cell with LBCF55 and LBCF28 cathode but the latter was unstable under a cathodic bias owing to the increase in ohmic resistance owing to the production of intermediate

layer between electrode and electrolyte. With better stability than LBCF28 and higher performance than LBC, LBCF55 was regarded as a viable cathode material for H-SOFC. This work explores systematically the behavior of a perovskite with mixed Cu and Fe cations as a cathode for H-SOFCs.

Keywords: H-SOFC, cathode, perovskite, durability, hydrogen energy.

1. Introduction

Solid oxide fuel cells (SOFCs) are all-solid chemical power-generation devices that can convert the chemical energy stored in fuel into electrical energy with high efficiency [1, 2]. Compared with the traditional oxygen ion-conducting solid oxide fuel cells, proton-conducting solid oxide fuel cells (H-SOFCs) having a lower operating temperature would decrease the degradation of the cell component due to the high-temperature oxidation of metal structures and deactivation of electrocatalyst [3, 4]. At a reduced temperature, the polarization loss on the cathode-electrolyte interface would be the predominant factor limiting the electricity output of H-SOFCs [5]. Therefore, the optimization of the cathode materials could be critically important to reduce the polarization loss of the cell and increase the power output of the H-SOFC at a reduced temperature [6, 7].

The perovskite structure oxide with the general formula ABO_3 could tolerate different types of cations to tune the electric and ionic conductivity, and electrocatalysis for the oxygen reduction reaction (ORR) on the cathode [8, 9]. There are similar importance in the ORR on the cathode side between the protonic conduction and oxide-ion conductivity [10]. Perovskite-type cobaltites showed superior ionic conductivity and catalytic activity toward ORR, whereas the much higher thermal expansion coefficient (TEC) values than the electrolyte and possible phase transition could limit the durability of the cell [11-13]. In addition, the effort to search for low-cost cathode material than cobaltite also stimulates the search for cobalt-free cathodes [14-16].

Both cuprate and ferrite-based perovskite oxides have been studied as the electrocatalysts for the ORR at reduced temperature [17, 18]. $La_{1.5}Ba_{1.5}Cu_3O_{7\pm\delta}$ showed a polarization resistance (R_p) of 0.041 Ω cm^2 at 700 ^{o}C on Sr- and Mg- codoped $LaGaO_3$ electrolyte while $Pr(Pr_{0.5}Ba_{1.5})Cu_3O_{7-\delta}$ reacted with $Sm_{0.2}Ce_{0.8}O_{2-\delta}$ to produce a composite of perovskite and fluorite for excellent ORR on BCZY electrolyte[7, 19]. $Ba_2YCu_3O_{7-\delta}$ (BYC) has been studied as a cathode for an H-SOFC, and the $Fe^{3+/4+}$ as a donor to dopant on $Cu^{2+/3+}$ was used to increase its oxygen content [20, 21]. $RBaCuMO_5$ (R=rare-earth element, M=Fe and Co) having a layered perovskite-type structure [22, 23] was reported to facilitate oxygen diffusion and further enhance the cathode performance of the SOFC [24-26]. The increase of iron ions content can increase the oxygen vacancy ($V_O^{\cdot\cdot}$) concentration of the material, and the lower bond energy of Cu-O compared with Fe-O bonds reduces the bonding strength of oxygen ions, making it easier to migrate, thereby increasing oxygen ions permeability [12]. $LaBaCuFeO_{5+\delta}$ have been studied as a potential SOFC cathode of a cell with SDC ($Sm_{0.2}Ce_{0.8}O_{1.9}$) or BCZY electrolyte , but no stability was reported in either research under a bias [26, 27]. The properties of the perovskite in terms of conductivity, stability and electrocatalysis with varying ratios of $Cu^{2+/3+}$ and $Fe^{3+/4+}$ needs to be optimized under the actual H-SOFC working conditions.

In this work, $La_{0.5}Ba_{0.5}Cu_xFe_{1-x}O_{3-\delta}$ ($0 \le x \le 1$) varying the Cu/Fe ratio on the B site were explored to find an optimized cathode for H-SOFC. The mixed Cu and Fe would increase the conductivity of the perovskite compared those with either Fe or Cu alone. The $La_{0.5}Ba_{0.5}Cu_{0.5}Fe_{0.5}O_{3-\delta}$ (LBCF55) cathode maintained a good stability, specifically, the R_p increased slightly from 0.065 Ω cm^2 to 0.068 Ω cm^2 at 700 ^{o}C for 60 hours. The superficial decomposition of the perovskites causing the increase in the ohmic resistance (R_s) could be the reason for the degradation of the cell, but does not increase the R_p of the cell.

2. Experimental

2.1 Materials preparation

$La_{0.5}Ba_{0.5}Cu_xFe_{1-x}O_{3-\delta}$ ($0 \le x \le 1$) perovskites were synthesized by the combustion method. When x is equal to 0, 0.2, 0.4, 0.5, 0.6, 0.8 and 1, the oxide is denoted as LBF, LBCF28, LBCF46, LBCF55, LBCF64, LBCF82 and LBC. Stoichiometric amounts of $La(NO_3)_3 \cdot 6H_2O$ (99.9% Macklin, China), $BaCO_3$ (99.99% Aladdin, China), $Cu(NO_3)_2 \cdot 3H_2O$ (99% Macklin, China), $Fe(NO_3)_3 \cdot 9H_2O$ (99.9% Aladdin, China) were dissolved in diluted HNO_3 (5 wt.% in deionized water). Citric acid (a molar ratio of metal cation: citric acid = 2:3) was then added as complexing agent. The admixture was heated on a hotplate until the water evaporated continuously to form a gel that was ignited at 350 ºC to induce a self-propagating combustion. The powder was calcined in a muffle furnace at 600 ºC for 2 hours first and then 920 ºC for 6 hours to obtain the perovskite powder. The powder calcined at 600 ºC were ground pressed under 20 MPa pressure, and calcined at 920 ºC for 6 hours for the dense pellet for the conductivity and thermal expansion coefficient (TEC) measurement.

$BaZr_{0.1}Ce_{0.7}Y_{0.2}O_{\delta}$ (BZCY) electrolyte powder and 65 wt.% NiO–$BaZr_{0.1}Ce_{0.7}Y_{0.2}O_{\delta}$ (NiO-BZCY) anode powder were synthesized by the citric acid-nitrate combustion method [7]. $BaCO_3$ (99.99% Aladdin, China), $Zr(CH_3COO)_4$ (Zr, 15.0-16.0 %, Macklin, China), $Ce(NO_3)_3 \cdot 6H_2O$ (99.95 %, Macklin, China), Y_2O_3 (99.9 %, Macklin, China) and $Ni(CH_3COO)_2 \cdot 4H_2O$ (99.9 %, Macklin, China) served as the raw materials for BZCY powder. The powders were calcined in a muffle furnace at 600 ºC for 3 hours firstly and then 1000 ºC for 5 hours to obtain BZCY and NiO-BZCY powders.

2.2 Characterization

The phase structure of the samples was analyzed using a diffractometer (Cu $K_{\alpha 1}$ =1.54056 Å, Persee XD-3, China) in the 2θ range from 10º to 80º at a step size of 0.02º in a reflective mode. The

pellets of the samples were cut into a rectangular bar (3×3×12 mm in size), and the direct current (DC) four-probe conductivity was measured on a high-precision multimeter (Keithley 2100, USA). A dilatometer (PCY-1400II, Xiangtan, China) was used to measure the thermal expansion coefficient (TEC) and isothermal chemical expansion of the bar-shaped sample (4×8×20 mm). The thermogravimetric analysis (TGA) in the air was carried out by a TG209 F3 tarsus instrument (NETZSCH, Germany). X-ray photoelectron spectroscopy (XPS) of the cathode surface after the fuel-cell durability test was collected on a K-Alpha spectrometer (Al K_α radiation, Thermo Fisher, USA).

The proton conductivity was obtained by blocking-electrode method using alternate current (AC) impedance measurement method. The BZCY and LBCF55 pellets were polished to 0.5 mm in thickness. The LBCF55 pellet was sandwiched between to two BZCY pellets. Silver wire was attached to the BZCY surface using the silver paste for the current collection. The total resistance of the sandwich was measured using a Chroma 2302 LCR meter in the frequency range from 20 to 1M Hz and the resistance of LBCF55 was calculated by the deduction of the resistance of two BCZY pellets. The proton conductivity of LBCF55 was then calculated based on the resistance and geometry of the LBCF55 pellet. Similar operations were done on LBCF28 and LBC.

Electrical conductivity relaxation (ECR) was used to evaluate the oxygen transport characteristics of a sample at a specific temperature using four-probe DC conductivity under a sudden change of partial pressure of oxygen $P(O_2)$. A mass flow controller was used to modify the $P(O_2)$ in the environment around the sample by mixing proportionate air and Ar. After a fast change in $P(O_2)$ from 0.21 to 0.02 atm., record the transient conductivity, normalize it using equation (1) [28], then fit the solution of Fick's second law to get the chemical surface exchange coefficient (K_{chem}) and chemical diffusion coefficient (D_{chem}) [29] using an ECRTOOLS [30] code in MATLAB toolbox. The derivation

process of the relevant equations was shown in equations (1-6) in supporting information.

$$g(t) = \frac{\sigma_{(t)} - \sigma_0}{\sigma_\infty - \sigma_0} \qquad (1)$$

where $g(t)$ is the normalized conductivity, σ_0 is the initial conductivity, $\sigma_{(t)}$ is the instantaneous conductivity at time t after $P(O_2)$ abrupt change, and σ_∞ is the equilibrium conductivity for a given $P(O_2)$.

2.3 Cell Fabrication and Testing

To make a NiO-BZCY|BZCY half-cell green body, co-press a suitable amount of NiO-BZCY powder and BZCY powder, then sinter it at 1320 ºC for 5 hours. The slurry was painted on the side of the BZCY and sintered at 970 ºC for 5 hours. To collect the current, the silver wire was attached to the electrode with silver paste containing 20 % starch. The cell was sealed to the ceramic tube with high-temperature inorganic adhesive (S525 SINWE, China), and the test device was heated to the desired temperature in a tube furnace. The electrochemical impedance spectroscopy (EIS) and current-voltage (I-V) of the produced fuel electrode were measured in the temperature range of 500 ºC-700 ºC after H_2 (25 mL min^{-1}) was supplied into the anode chamber as fuel.

All electrochemical measurements were performed in the frequency range of 1 MHz to 0.1 Hz on a Zennium *Pro* electrochemical workstation (Zahner, Germany). The sine wave for EIS was 10 mV in amplitude, and the EIS data were fitted using Z-man software.

2.4 Density Functional Theory (DFT) calculations.

DFT calculations were conducted using the QUANTUM ESPRESSO package. The projector augmented wave (PAW) was used simulating the electron-ion interactions. The Perdew-Burke-Ernzerhof (PBE) functional was used as an exchanged-correlation functional approximation. A k-point mesh of 3 × 3 × 3 and a cutoff energy of 49 and 591 Ry for the charge-density cutoff were selected.

The bulk LBC was represented by a cubic unit cell (7.81 × 7.81 × 7.81 Å) which contains 40 atoms in a (2 × 2 × 2) supercell. The model of $La_4Ba_4Cu_8O_{24}$ was built to simulate the bulk of the LBC perovskite. The LBF and LBCF materials were modeled by replacing 8 Cu atoms and 4 Cu atoms of LBC to Fe and noted as $La_4Ba_4Cu_4Fe_4O_{24}$ and $La_4Ba_4Fe_8O_{24}$ respectively. For the calculation of oxygen vacancy formation, one of the center oxygen atoms was removed to mimic the $V_O^{\cdot\cdot}$ and all the layers were relaxed. The central oxygen atom was selected to avoid the boundary effect.

The calculation equation of $V_O^{\cdot\cdot}$ formation energy (E_{vo}) was shown as formation (2)

$$E_{vo} = (E_{vac} + 1/2E_{O2}) - E_{opt} \quad (2)$$

where E_{vac} is the total energy of the supercell containing an $V_O^{\cdot\cdot}$, E_{O2} is the energy of an isolated oxygen molecule, and the E_{opt} is the energy of optimized perfect supercell [31].

3. Results

XRD (Fig 1(a)) of $La_{0.5}Ba_{0.5}Cu_xFe_{1-x}O_{3-\delta}$ (x=0, 0.2, 0.4, 0.5, 0.6, 0.8, 1) series were single-phase perovskite at room temperature. All powders exhibited an orthorhombic structure except for a cubic LBF, which is consistent with previous reported by others [26, 32]. The unit cell parameters (Table 1) of the perovskites containing Fe showed an *Immm* symmetry. The axial distortion in the copper and iron coordination polyhedra, as well as the equatorial oxygen atom distortion, are the key hallmarks of this structure [33]. The cell volume gradually increases with Cu^{2+} from LBF to LBCF28 and then it starts to decrease. The increase of cell volume from LBF to LBCF28 could be a result of the reduction of Fe^{4+} to Fe^{3+} or the incorporation of Cu^{3+} and Cu^{2+} with a larger cation radius than Fe^{4+} and Fe^{3+}, respectively. According to the previous research based on Mossbauer spectroscopy and susceptibility on LBCF [34], the Cu doping at $x < 0.2$ will cause the increase in Fe^{4+}. Therefore, we think the expansion could be related to the incorporation of large $Cu^{3+/2+}$ in the perovskite lattice. With $x > 0.4$,

the increase of oxygen vacancies will cause contraction of the cell volume [35]. When x ⩽ 0.4, there could be an increase in the percentage Fe^{4+} and Cu^{3+} out of the total cations, which is consistent with the extraordinarily high conductivity of LBCF28 and LBCF46.

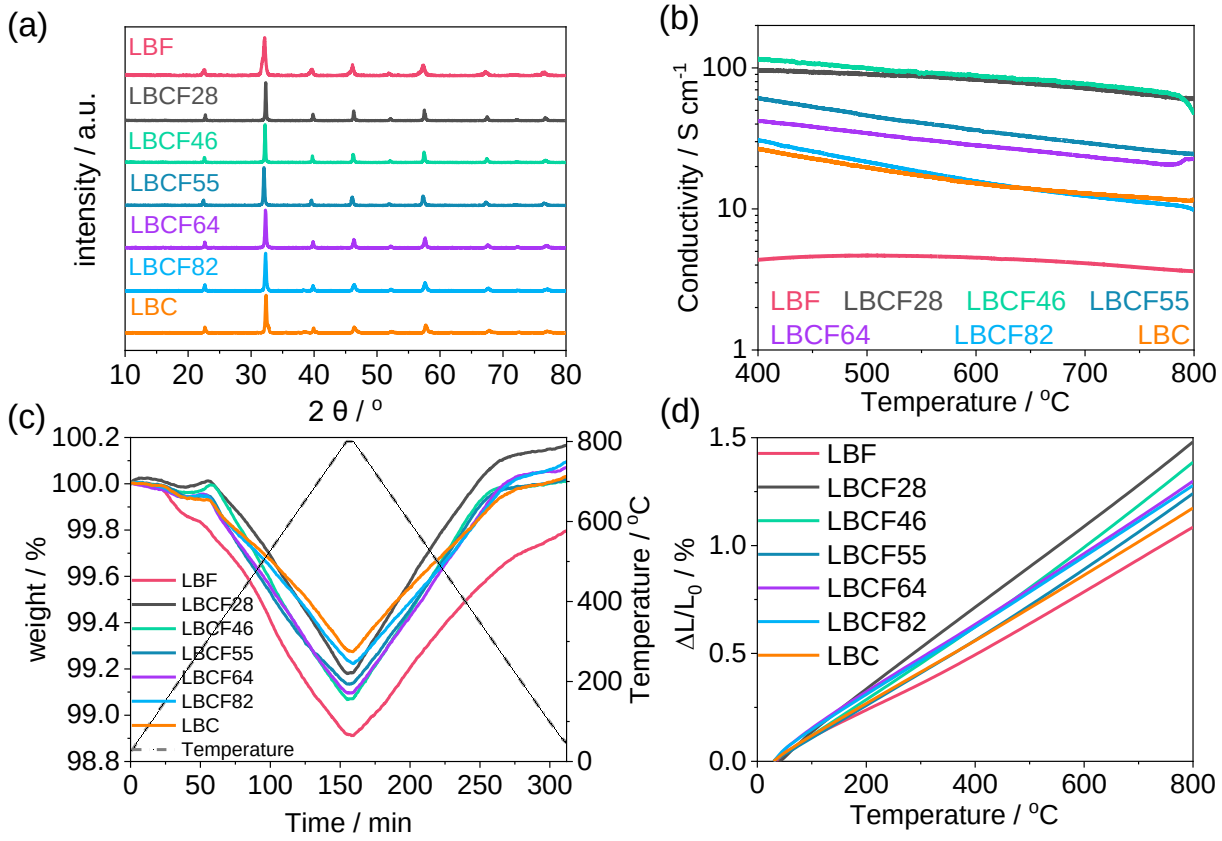

Fig 1. (a) XRDs, (b) electric conductivities, (c) TGA and (d) thermal expansion of $La_{0.5}Ba_{0.5}Cu_xFe_{1-x}O_{3-\delta}$ (x=0, 0.2, 0.4, 0.5, 0.6, 0.8, 1) in air.

Table 1

Thermal expansion and the room-temperature unit cell parameters.

Composition	Acronym	TEC	Symmetry	Lattice parameter			V^d
		ppm K^{-1}		*a* / Å	*b* / Å	*c* / Å	$Å^3$
$La_{0.5}Ba_{0.5}FeO_3$	LBF	14.19	Pm3m	3.9331(5)	3.9331(2)	3.9331(2)	60.84
$La_{0.5}Ba_{0.5}Cu_{0.2}Fe_{0.8}O_3$	LBCF28	19.48	Immm	5.5698(4)	5.5559(6)	7.8859(2)	61.01

$La_{0.5}Ba_{0.5}Cu_{0.4}Fe_{0.6}O_3$	LBCF46	18.00	Immm	5.5505(5)	5.5592(1)	7.8530(7)	60.58
$La_{0.5}Ba_{0.5}Cu_{0.5}Fe_{0.5}O_3$	LBCF55	16.12	Immm	5.5772(4)	5.5632(4)	7.8064(8)	60.56
$La_{0.5}Ba_{0.5}Cu_{0.6}Fe_{0.4}O_3$	LBCF64	16.86	Immm	5.5401(5)	5.5337(3)	7.8340(6)	60.04
$La_{0.5}Ba_{0.5}Cu_{0.8}Fe_{0.2}O_3$	LBCF82	16.61	Immm	5.5262(8)	5.5352(8)	7.8297(1)	59.88
$La_{0.5}Ba_{0.5}CuO_3$	LBC	15.25	Pmmm	3.8944(6)	3.9097(3)	11.7438(5)	59.61

d: pseudo-cubic cell volume for comparison.

The electric conductivity (Fig 1(b)) of the oxides with mixed Fe and Cu was significantly higher than those of LBF and LBC and the highest conductivity was obtained on LBCF46, reaching 75-80 S cm^{-1} at 600-700 ^oC. The TGA at 800 ^oC in flowing air (Fig 1(c)) was used to explore the stability. The actual loss of oxygen from the oxide lattice could be minor blow 300 ^oC and the obvious weight loss of LBF could be attributed to the loss of adsorbed CO_2 or H_2O. The oxygen loss started at 300 ^oC and was generally reversible for all the oxides except for LBF. The irreversible oxygen loss of LBF could be accounted for by the weight loss below 300 ^oC though the cation ordering on A-site was found to be important to the oxygen stoichiometry of the perovskite-type ferrite [36].

Thermal expansion coefficient (TEC) is one of the key factors that would affect the durability of the cell during the thermal cycles. The mismatch in TEC between the electrolyte and electrode material will cause crack and delamination on the interface [37]. The dilatometry up to 800 ^oC (Fig 1(d)) showed a linear curve and the TEC value of the LBC and LBF samples were 15.25 and 14.19 ppm K^{-1}, respectively. However, the TEC of LBF could also be 19.4 ppm K^{-1} in an oxygenated condition [38] and the difference could be related to the difference in the oxygen content. The TEC of LBCF55 is 16.12 ppm K^{-1}, which is closer to that of the electrolyte BZCY of 10.1 ppm K^{-1} [39] than the other

compositions with mixed Cu/Fe cation. The higher Fe^{4+} concentration in $Ln_{0.5}Ba_{0.5}FeO_{3-\delta}$ (Ln= La, Pr, Nd, Sm, Gd and Y) increase with the TEC [38] and the thermal reduction of Fe^{4+} will add to the chemical expansion [40]. With the doping of Cu, the decrease in the [Fe^{4+}] against the total B-site cation could be the reason for the lower TEC of LBCF55 than LBCF28 and LBCF46. Actually for those with $x \geq 0.5$, the TECs are actually close becaused of the reduced [Fe^{4+}].

The chemical expansion of the perovskite is also important for the stability of the cathode that could be subjected to the negative bias. Isothermal dilatometry (Fig 2(a, b)) indicated that the $P(O_2)$ decrease from 0.21 to 0.02 atm. caused an expansion, and *vice versa*. The maximum expansion of LBC was only 0.004 % and 0.005 % at 600 ℃ and 700 ℃, respectively, which was only one-tenth that of LBCF28 (0.043 % and 0.075 % at 600 ℃ and 700 ℃, respectively). However, when the gas was restored to air, LBCF28 did not shrink to the original size in 30 minutes which was a sign of destruction of the structure. On the other hand, LBC and LBCF55 could shrink to the original size or smaller in 30 minutes because Cu ion in the square planar <CuO_4> could change readily to <CuO_5> pyramid with oxide-ion intercalation, similar to $Ba_2YCu_3O_{6+\delta}$, with slower kinetics during lattice expansion than during contraction [41].

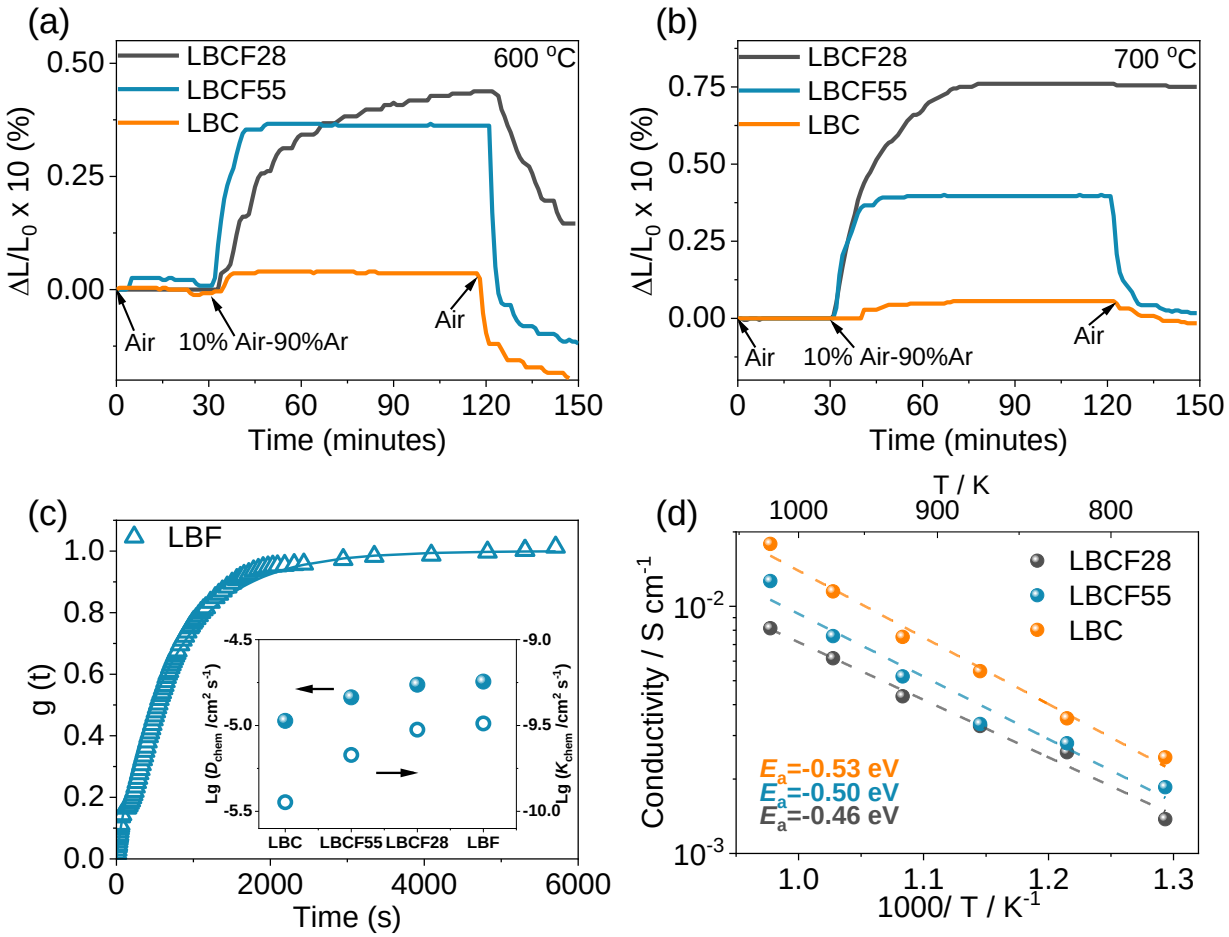

Fig 2. Isothermal dilatometry of LBC, LBCF55 and LBCF28 under switching air and 10% air-90% Ar at 600°C (a) and 700 °C (b). ECR of LBF (c) at 700 °C after a $P(O_2)$ step adjustment from 0.21 to 0.02 atm.. The solid lines represent the corresponding fit to the measured data. (d) Proton conductivity of LBCF28, LBCF55 and LBC measured using blocking electrode. The inset in (c) shows the fitted D_{chem} and K_{chem} of LBC, LBCF55, LBCF28 and LBF at 700 °C.

The oxygen surface exchange coefficient (K_{chem}) and bulk diffusion coefficient (D_{chem}) were calculated using the ECR method [42] to probe the oxygen transport property [43]. When the $P(O_2)$ was decreased from 0.21 to 0.02 atm. at 700 °C, and the normalized conductivity over time for LBF as an example was shown in Fig 2(c). The D_{chem} and K_{chem} values were obtained by fitting the transient conductivity according to Fick's second law. D_{chem} and K_{chem} values increased with Fe content, and the former was always around 4-5 orders of magnitude greater than the latter . Compared with some typical

cathode materials, the D_{chem} value of sample was greater than that of $La_{0.6}Sr_{0.4}Co_{1-y}Fe_yO_{3-\delta}$ about 10^{-9}-10^{-8} cm^2 S^{-1}, and the value of K_{chem} was similar to each other [44, 45]. It confirms that LBCF with remarkably fast surface oxygen exchange and good oxygen ion diffusion properties at intermediate temperatures.

The proton conductivities of the samples (Fig 2(d)) measured by AC impedance method in air was positively correlated with temperature. In the same time, they decreased with increasing Fe content. The estimated activation energy (E_a) of LBCF28, LBCF55, and LBC was 0.53, 0.50, and 0.46 eV, respectively, by the linear fittness. Overall, LBC sample possesses high σ_H and low activation energy.

The current-voltage (I-V) and current-power (I-P) curves (Fig 3(a-c)) of the single cells at the first hour at different temperatures indicated that the open circuit voltages (OCVs) were higher than the srandard voltage with BZCY as electrolyte, 1.0 V, showing that the electrolyte was airtight and the gas crossover was minor. The peak power densities of the three full cells with LBCF28, LBCF55, and LBC at 700 ^oC were 822, 820, and 650 mW cm^{-2}, respectively. The current densities (Fig 3(d)) at 0.6 V showed an overall decrease along with time at 700 ^oC. The cell with LBCF55 and LBCF28 showed a similar current density within the first 5 hours, while the current density of the LBCF55 cell decreased gradually, the one with LBCF28 degraded dramatically in the 5 to 24 hours and recover slightly to reach a stable current density at 60 hours. Although the cell with LBC decreased slightly, the current density in the time scope was lower than the one with LBCF55. The cell with LBF (Fig S1) yield bad performance due to the low electric conductivity, while the cell with LBCF46 (Fig S2) showing highest conductivity showed a similar performance to the one with LBC cathode.

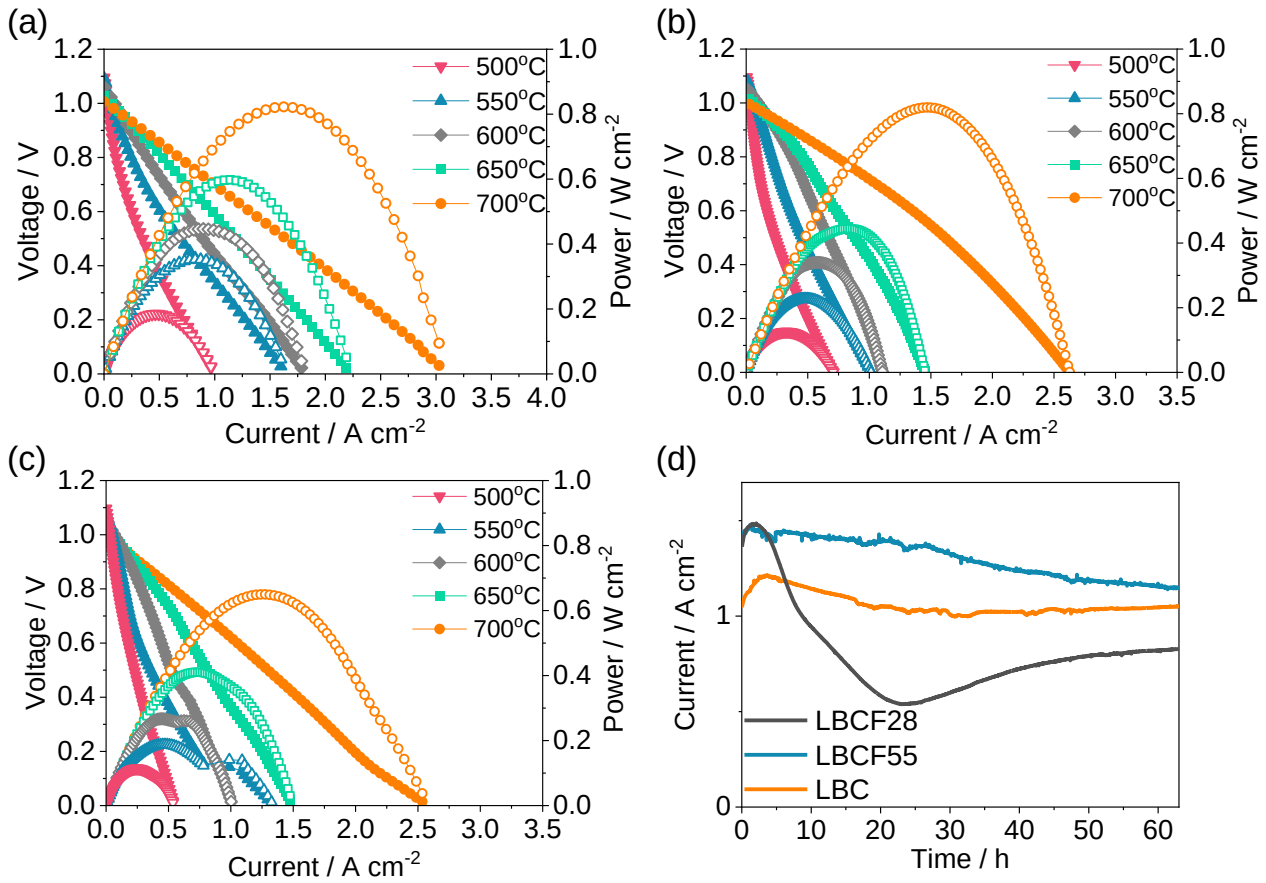

Fig 3. I-V (filled marks) and I-P (open marks) curves of single cell (a) LBCF28|BZCY|NiO-BZCY, (b) LBCF55|BZCY|NiO-BZCY and (c) LBC|BZCY|NiO-BZCY at different temperatures. (d) The evolution of current density of cells with LBCF28, LBCF55 and LBC cathodes at 700 °C. The durability tests were repeated twice to check the validity of the results.

The area-specific resistance (ASR) of the three cells all decreased with the temperature (Fig S3), indicating that the electrochemical reaction was a thermal activation process. The polarization resistance (R_p) of the cell with LBCF55 as the cathode (Fig S4) reduced from 2.397 Ω cm^2 to 0.065 Ω cm^2 from 500 °C to 700 °C, and ohmic resistance (R_s) decreased from 0.451 Ω cm^2 to 0.198 Ω cm^2. The ratio of R_p/R_t (total resistance) decreased from 84.2% at 700 °C to 24.7% at 500 °C, which meant R_p was pre-dominant in reduction of the R_t at temperature below 600 °C.

The EIS of the cells before and after chronoamperometry test (Fig 4(a)) for 60 hours at 700 ℃

were used to probe the degradation mechanism under the cathodic bias in the fuel cell mode.The ASR of the cells after the durability test was in the sequence LBCF55 (0.308 Ω cm^2) < LBC (0.336 Ω cm^2) < and LBCF28 (0.386 Ω cm^2) ,which is consistent with the initial cell performance. The EIS were fitted with two Voigt elements and the graph of the equivalent circuit is shown in Fig 4(b). The resistances (Fig S5) for the arc at the the high-frequency arc (R_1) and the low-frequency (R_2) were linked to charge transfers and adoroption and dissociation of O_2 molecules, respectively [46]. The R_1 of the cells with LBCF28 and LBC increased after durability test (0.025 and 0.008 Ω cm^2), while the one with LBCF55 increased slightly (0.007 Ω cm^2). On the other hand, the R_2 of the LBCF28 and LBC cell dcreased during the durability, but the one of LBCF 55 cell maintained a stable value. The decreased in R_2 accounts for the R_p decreased in the LBC cell.

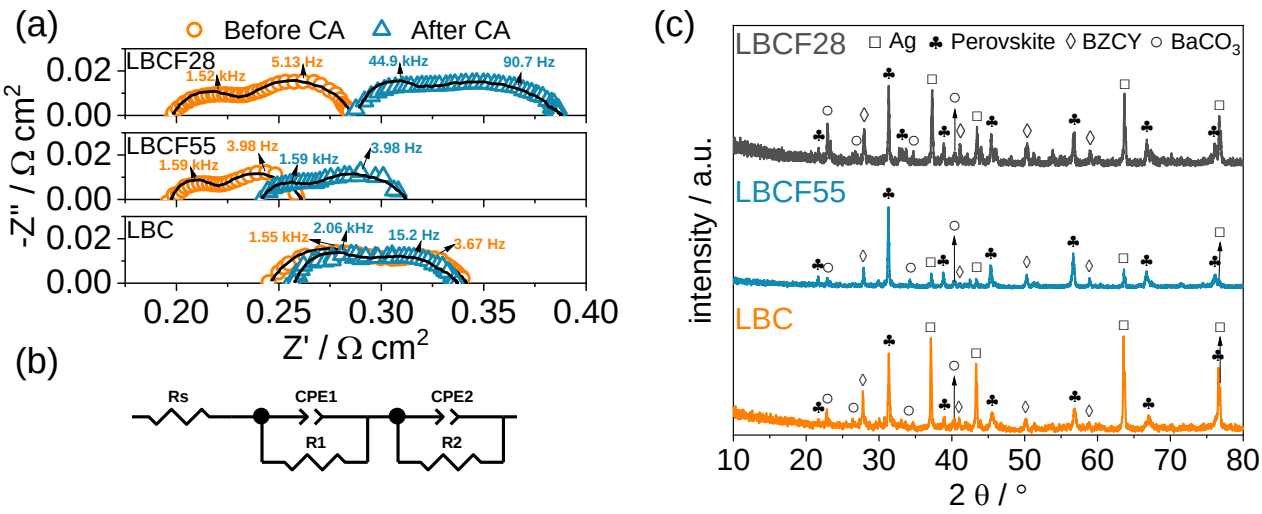

Fig 4. (a) EIS for the cells with LBCF28, LBCF55 and LBC at 700 ºC before and after chronoamperometry. The black line is the fitted data with two Voigt elements. (b) Graphical representation of the equivalent circuit for the fitting of EIS. (c) XRDs of LBCF28|BZCY|NiO-BZCY, LBCF55|BZCY|NiO-BZCY and LBC|BZCY|NiO-BZCY cells after testing at 700 ºC.

After chronoamperometry test at 700 ºC, the cathode materials on BZCY electrolyte maintained the perovskite structure for all the three cells (Fig 4(c)), but surface decomposition producing $BaCO_3$

was observed. However, the relative intensity of $BaCO_3$ on the LBCF55 surface was much weaker than the other two. After the 120-hour calcination at 700 ºC at OCV, the XRDs (Fig S6) of LBCF28, LBCF55, and LBC showed good stability, and no $BaCO_3$ was found in the XRDs. The comparison of the phase composition of the cathode under load and at OCV indicated that the transport of protons and application of cathodic bias posed great exertion on the stability of the cathode.

As the electrochemical process takes place on the very surface of the cathode and XPS (Fig 5) was used to further study the superficial properties of the electrode after the durability at 0.6 V. A full spectral scan of the XPS spectrum was performed in the range of 0-1350 eV, and the peaks for La, Ba, Cu, Fe, O and C peaks were found (Fig 5(a)). The XPS spectrum of Ba $3d_{5/2}$ (Fig 5(b)) showed two splits at 780.0 and 778.1 eV were assigned to $BaCO_3$ and perovskite, respectively [47, 48]. The absence of Ba $3d_{5/2}$ peaks for perovskite indicated the severe decomposition of LBC, which is consistent with the high ohmic loss the cell with this cathode. The core-level scan of C 1s (Fig 5(c)) could be decomposed into a triad of sp^3 C (284.8 eV), C-O group (286.0 eV) and C=O group (289.1 eV) of carbonate a peak [49]. In LBC, the Cu $2p_{3/2}$ spectrum was represented by Cu^+, Cu^{2+} and Cu^{3+} peaks with binding energies of 931.8, 933.5 and 935.5 eV, respectively [50, 51], but the spilt for Cu^{3+} disappeared as a result of the inclusion of Fe^{3+} [52]. The core-level scan for Fe 2p indicated the presence of Fe^{2+} after the durability test in both LBCF55 and LBCF28, which could be linked to the reduction of Fe^{3+} and Fe^{4+} under a cathodic bias [53, 54]. The increase of Cu as an acceptor will reduce the valence of Fe in the oxygenated perovskite. Due to the three-dimensional interaction between copper ions, Cu^{3+} is formed through partial saturation of Fe^{4+} atomic energy levels, and then Fe^{4+} is reduced to Fe^{3+} through redox equilibrium [34]. The fitting results of Cu 2p and Fe 2p XPS spectra were shown in Fig 5(d, e) and Table S1. The peak (Fig 5(f)) at 528.6 eV and 531.6 eV in the O 1s XPS

spectra can be attributable to lattice oxygen (M-O) and oxygen vacancies, respectively, while the splitting of the binding energy of O 1s at 533.1 eV in LBC was attributed to C=O species [55, 56] as a result of the surface decomposition.

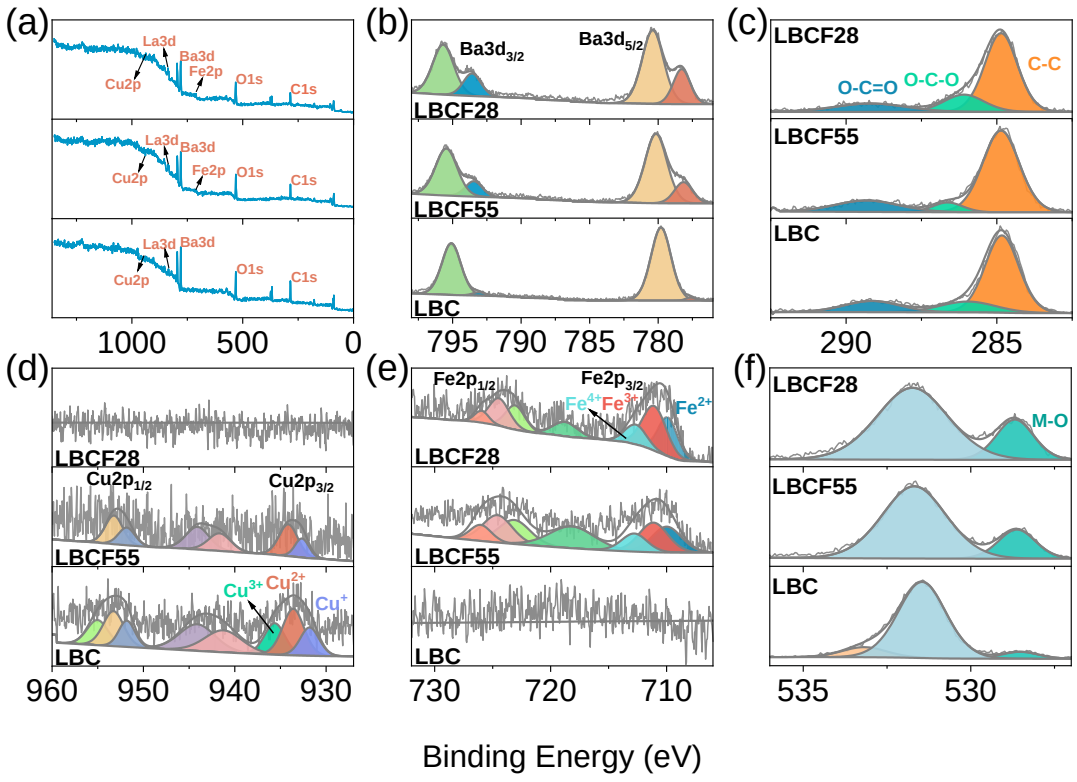

Fig 5. XPS of LBCF28, LBCF55, LBC after the fuel-cell durability test: (a) overview survey and the high-resolution core-level scans of (b) Ba 3d, (c) C 1s, (d) Cu 2p, (e) Fe 2p and (f) O 1s.

Cross-section SEM (Fig 6(a-c)) of the LBCF28 and LBC cell after the durability test revealed a dense barrier layer between the electrode and the electrolyte that is absent in the one for the cell with LBCF55 cathode. The LBCF55 cathode was a uniform porous structure, and the particles connected to each other and adhered to the electrolyte. The composition of the dense layer (around 2 mm in LBCF28 and) on the electrolyte was found to be Zr and Y enriched layer (Fig S7), which is consistent with the ohmic loss in the cell with LBCF28 and LBC cathode. In some places of the LBCF28 cathode (Fig S7), large $BaCO_3$ particles could reside above the zirconia-rich dense layer, cuasing the

delamination of the electrode from the electrolyte. The dense layer could be related to the decomposition of the electrolyte. In the higher-magnification image of the cathode (Fig 6(d-f)), there were fine particles (< 200 nm) outgrown on the surface of the grains of perovskite. According to the XPS and XRD analysis, this fine particle could be attributed to the $BaCO_3$ particles.

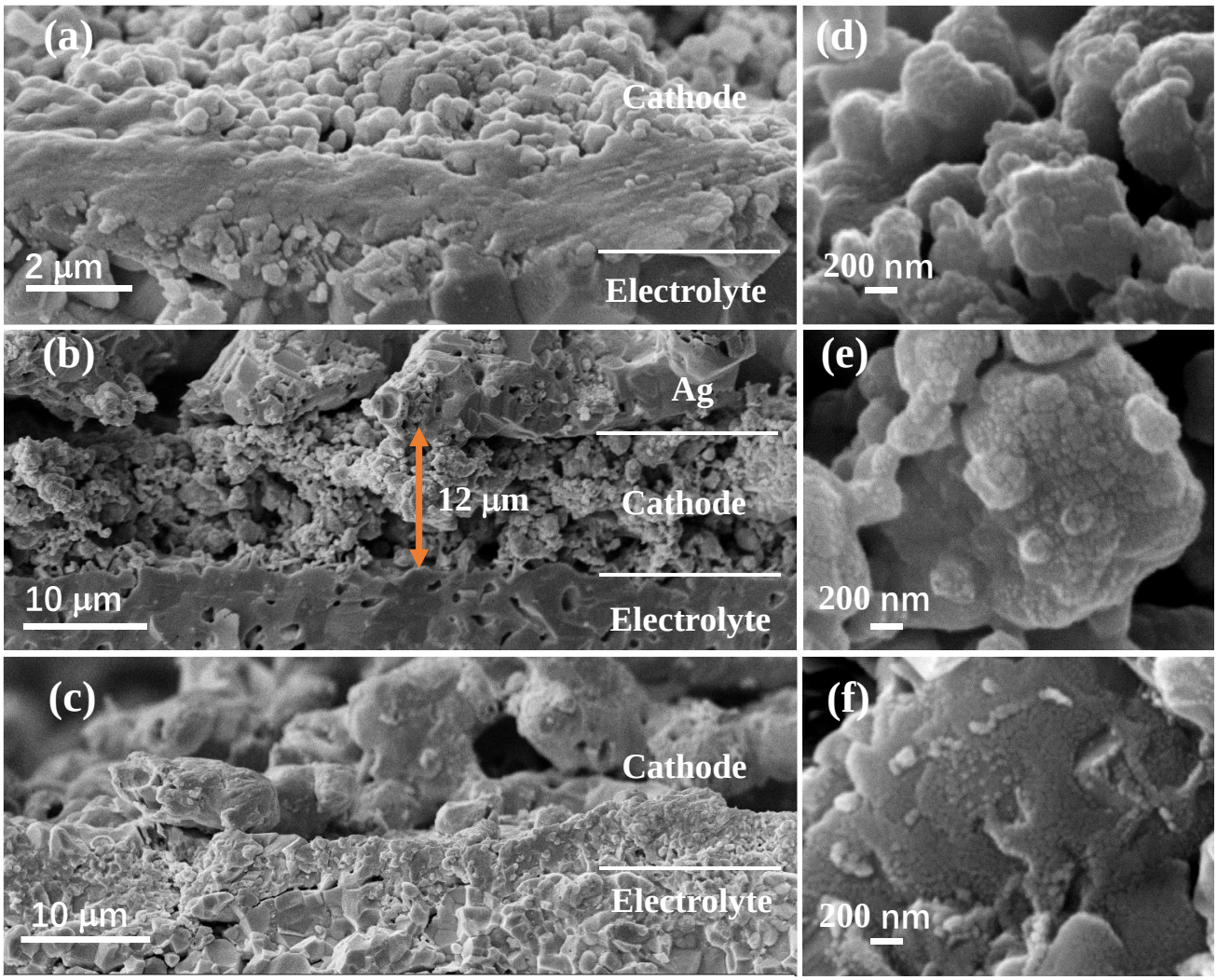

Fig 6. Cross-section SEM image of the (a) LBCF28, (b) LBCF55 and (c) LBC cell after durability testing for 60 hours, the enlarged SEM images of (d) LBCF28 (e) LBCF55, and (f) LBC cathodes after durability testing for 60 hours.

4. Discussion

The cathode reaction of an H-SOFC involves the adsorption, and dissociation of O_2 for the

300 production of O_{ads} that would react with $OH^{\cdot}$ (equation (3)) for the production of H_2O and $V_O^{\cdot\cdot}$ as a
301 result of the reduction of the perovskite [57]. The oxide-ion and protonic conductivity would be both
302 important for the reaction sites of the cathode.

303 $4OH_O^{\cdot} + O_2 + 4e^- = 2H_2O + 4\ O_O^x$ (3)

304 where Kröger-Vink notation is used.

305 As $OH_O^{\cdot}$ in solid phase is reacting with the gaseous O_2, the oxide-ion conductivity of the cathode
306 would be beneficial to the expansion of reaction sites and give room to the incorporation of O_O^x into
307 the perovskite for the structure stability. For the oxide-ion conductivity, the formation energies of one
308 $V_O^{\cdot\cdot}$ from $La_4Ba_4Cu_8O_{24}$ (LBC), $La_4Ba_4Cu_4Fe_4O_{24}$ (LBCF) and $La_4Ba_4Fe_8O_{24}$ (LBF) (Fig 7) indicates
309 that E_{vo} from 0.89 eV in LBC raised to 3.25 eV in LBF, which is in contrast with the trend of oxide-
310 ion conductivity. Moreover, in a mixed Cu/Fe perovskite, *e.g.* LBCF55, E_{vo} in the sequence of Fe-Vo-
311 Fe > Cu-Vo-Fe > Cu-Vo-Cu for a δ of 1/24. However, acceptor doping of $Cu^{3+/2+}$ in $La_{0.5}Ba_{0.5}FeO_3$
312 will increase the oxygen deficiency (δ): *e.g.* the δ in LBC in the air is close to 0.667 out of 3 as in
313 $La_{1.5}Ba_{1.5}Cu_3O_7$, which is equivalent to 5 oxygen vacancy out of 24. The further loss of oxygen will
314 induce a higher E_{vo}, which could explain the higher oxide-ion conductivity in the Fe-rich perovskite.
315 On the other hand, the high δ of cuprate is consistent with the high protonic conductivity: donor doping
316 of $Fe^{4+/3+}$ on $Cu^{3+/2+}$ would decrease the hydration and protonic conductivity of the mixed perovskite.

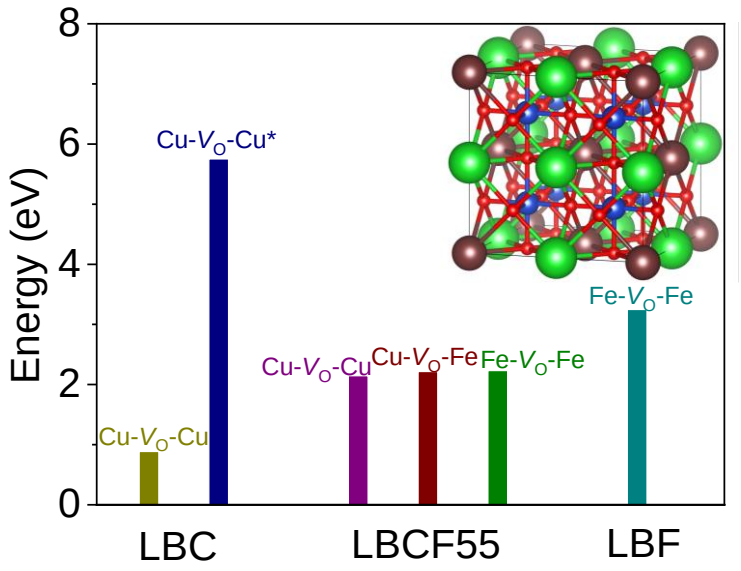

Fig 7. Formation energy of one oxygen vacancy from $La_4Ba_4Cu_8O_{24}$, $La_4Ba_4Cu_4Fe_4O_{24}$ and $La_4Ba_4Fe_8O_{24}$. The inset shows the $La_4Ba_4Cu_8O_{24}$ supercell model as an example. La, Ba, Cu, O atoms are in brown, green, blue and red, respectively; the Cu atom was substituted by Fe to form $La_4Ba_4Cu_4Fe_4O_{24}$ and $La_4Ba_4Fe_8O_{24}$ supercell models respectively. * represent two oxygen vacancies out of twenty-four oxygen sites.

The stability of superconducting $Ba_2YCu_3O_{7-\delta}$ is notoriously poor in highly humid conditions [58]: i.e. it tends to decompose at 85 °C and 85% relative humidity for the production of CuO, $Ba(OH)_2$ and O_2 as a result of the reduction of Cu^{3+} to Cu^{2+}. The stability of pure cuprates would be an issue if they were used as a cathode for the generation of H_2O under an reducing atmosphere. In the presence of CO_2 in the air, the production of $BaCO_3$ is foreseeable at a temperature of 700 ºC. The higher valence of $Fe^{4+/3+}$ doping was found to increase the stability of the LBCF55 and LBCF28 at OCV (Fig S6), but the high Fe content (e.g. LBCF28) was found to decrease the stability of the cathode under cathodic bias because the generated Fe^{2+} does not fit in the octahedron or pyramid in the perovskite, but is tending to generate a planar <FeO_4> [2, 49], causing the destabilization of the perovskite. The

instability from the dilatometry of LBCF28 indicate that the change to and for the planar <FeO4> and pyramid/octahedron is impossible in Fe-enriched sample in this study. Moreover, the low protonic conductivity of LBCF28 would decrease the functional area where protons would transport and restrict the combination of $OH^{\bullet}$ and O_2 to the very electrolyte/cathode interface, causing higher humidity in this region, accelerating the production of $Ba(OH)_2$ and the following $BaCO_3$.

According to the EIS, the increase in R_p is minor in the cell with LBC, LBCF55 and LBCF28 and most of the cells loss is from the ohmic resistance as a result of the instability of the perovskite. The segregation of insulating $BaCO_3$ along with the valence decrease in Cu and Fe cation would be detrimental to the conductivity of the electrode. However, the generation of nanoparticles of $BaCO_3$ was reported to improve the K_{chem} of the electrode for faster surface diffusion of oxide-ion, which could be the reason for the nearly unchanged R_p [59, 60]. The exsolution of $BaCO_3$ on LBC and LBCF28 under a 0.6 V bias was found to assist the adsorption and dissociation of O_2 molecules which could be related to the increase in K_{chem} and the surface area of the electrode. The increased ohmic resistance in LBCF28 could be related to the Zr-rich layer, blocking the transfer of electrons and protons.

5. Conclusions

Single-phase $La_{0.5}Ba_{0.5}Cu_xFe_{1-x}O_{3-\delta}$ oxides with various Fe content have been explored as a cathode material of H-SOFC. Their structure, chemical stability, electrical conductivity and electrocatalysis under a cathodic bias have been investigated to study the impact of Fe/Cu ratio on each performance. The value of TEC grows dramatically as the amount of Fe increases, as does the value of conductivity, while proton conductivity drops. The LBCF55 cathode material has good electrical conductivity and proton conductivity. The oxygen-transport kinetics using ECR measurements

discovered that LBCF55 had comparable oxygen transport and surface exchange kinetics to prototypical LSCF and BSCF. LBC is not stable in the air , while LBCF28 showed a superior conductivity and electro-catalysis at the beginning, but they showed dramatic degradation under a cathodic current. The interlayer between the electrolyte and the electrode could be the reason for the deterioration of the cell as ohmic resistance is the prior parameter for the cell loss. The layer between the electrode and electrolyte is rich in Zr and Y and the $BaCO_3$ particle could have caused the delamination of the electrode. At 700 ^oC, a peak output of 820 mW cm^{-2} is archived with the LBCF55 cathode showing an R_p of 0.068 Ω cm^2. The cell also maintained good stability under a bias of 0.6 V for 60 hours. LBCF55 with high conductivity showed a decent initial polarization resistance and good chemical stability as the cathode of an H-SOFC.

Declaration of Competing Interest

The authors have no conflict of interest to declare.

Acknowledgements

This work was supported by the National Natural Science Foundation of China (51702264) and Fundamental Research Funds for the central universities (SWURC2020002). This work is also supported by the Research Funding from S&T Committee from Chongqing Municipality (cstc2021ycjh-bgzxm0162) and Chongqing Technology and Business University scientific research project (1956017) and the Science and Technology Research Program of Chongqing Municipal Education Commission (Grant No. KJQN201900843). C.N. is also thankful to Bayu Young Scholar from Chongqing, and J.N. appreciates the support from the Chongqing Yingcai project.

References

[1] J.H. Myung, D. Neagu, D.N. Miller, J.T. Irvine, Switching on electrocatalytic activity in solid oxide cells, Nature, 537 (2016) 528-531.

[2] C. Ni, J. Zhou, Z. Zhang, S. Li, J. Ni, K. Wu, J.T.S. Irvine, Iron-based electrode materials for solid oxide fuel cells and electrolysers, Energy & Environmental Science, 14 (2021) 6287-6319.
[3] H. An, H.-W. Lee, B.-K. Kim, J.-W. Son, K.J. Yoon, H. Kim, D. Shin, H.-I. Ji, J.-H. Lee, A 5 × 5 cm^2 protonic ceramic fuel cell with a power density of 1.3 W cm^{-2} at 600 °C, Nature Energy, 3 (2018) 870-875.
[4] C. Duan, R.J. Kee, H. Zhu, C. Karakaya, Y. Chen, S. Ricote, A. Jarry, E.J. Crumlin, D. Hook, R. Braun, N.P. Sullivan, R. O'Hayre, Highly durable, coking and sulfur tolerant, fuel-flexible protonic ceramic fuel cells, Nature, 557 (2018) 217-222.
[5] C. Xia, Y. Mi, B. Wang, B. Lin, G. Chen, B. Zhu, Shaping triple-conducting semiconductor $BaCo_{0.4}Fe_{0.4}Zr_{0.1}Y_{0.1}O_{3-\delta}$ into an electrolyte for low-temperature solid oxide fuel cells, Nat Commun, 10 (2019) 1707.
[6] C. Duan, J. Tong, M. Shang, S. Nikodemski, M. Sanders, S. Ricote, A. Almansoori, R. O'Hayre, Readily processed protonic ceramic fuel cells with high performance at low temperatures, Science, 349 (2015) 1321-1326.
[7] J. Hou, L. Miao, J. Hui, L. Bi, W. Liu, J.T.S. Irvine, A novel in situ diffusion strategy to fabricate high performance cathodes for low temperature proton-conducting solid oxide fuel cells, Journal of Materials Chemistry A, 6 (2018) 10411-10420.
[8] P. Goel, S. Sundriyal, V. Shrivastav, S. Mishra, D.P. Dubal, K.-H. Kim, A. Deep, Perovskite materials as superior and powerful platforms for energy conversion and storage applications, Nano Energy, 80 (2021).
[9] J. Hwang, R. Rao Reshma, L. Giordano, Y. Katayama, Y. Yu, Y. Shao-Horn, Perovskites in catalysis and electrocatalysis, Science, 358 (2017) 751-756.
[10] Y. Bu, S. Joo, Y. Zhang, Y. Wang, D. Meng, X. Ge, G. Kim, A highly efficient composite cathode for proton-conducting solid oxide fuel cells, Journal of Power Sources, 451 (2020).
[11] F. Liang, H. Jiang, H. Luo, J. Caro, A. Feldhoff, Phase Stability and Permeation Behavior of a Dead-End $Ba_{0.5}Sr_{0.5}Co_{0.8}Fe_{0.2}O_{3-\delta}$ Tube Membrane in High-Purity Oxygen Production, Chemistry of Materials, 23 (2011) 4765-4772.
[12] Z. Liu, K. Li, H. Zhao, K. Świerczek, High-performance oxygen permeation membranes: Cobalt-free $Ba_{0.975}La_{0.025}Fe_{1-x}Cu_xO_{3-\delta}$ ceramics, Journal of Materiomics, 5 (2019) 264-272.
[13] D. Garcés, A.L. Soldati, H. Troiani, A. Montenegro-Hernández, A. Caneiro, L.V. Mogni, La/Ba-based cobaltites as IT-SOFC cathodes: a discussion about the effect of crystal structure and microstructure on the O_2-reduction reaction, Electrochimica Acta, 215 (2016) 637-646.
[14] A. Ndubuisi, S. Abouali, K. Singh, V. Thangadurai, Recent advances, practical challenges, and perspectives of intermediate temperature solid oxide fuel cell cathodes, Journal of Materials Chemistry A, 10 (2022) 2196-2227.
[15] M. Wu, H. Cai, F. Jin, N. Sun, J. Xu, L. Zhang, X. Han, S. Wang, X. Su, W. Long, L. Wang, L. Zhang, Assessment of cobalt–free ferrite–based perovskite $Ln_{0.5}Sr_{0.5}Fe_{0.9}Mo_{0.1}O_{3-\delta}$ (Ln = lanthanide) as cathodes for IT-SOFCs, Journal of the European Ceramic Society, 41 (2021) 2682-2690.
[16] H. Wang, C. Tablet, A. Feldhoff, J. Caro, A Cobalt-Free Oxygen-Permeable Membrane Based on the Perovskite-Type Oxide $Ba_{0.5}Sr_{0.5}Zn_{0.2}Fe_{0.8}O_{3-\delta}$, Advanced Materials, 17 (2005) 1785-1788.
[17] M. Lefèvre, E. Proietti, F. Jaouen, J.-P. Dodelet, Iron-Based Catalysts with Improved Oxygen Reduction Activity in Polymer Electrolyte Fuel Cells, Science, 324 (2009) 71-74.
[18] A. Ramkiran, D.-V.N. Vo, M.S. Mahmud, Syngas production from ethanol dry reforming using

Cu-based perovskite catalysts promoted with rare earth metals, International Journal of Hydrogen Energy, 46 (2021) 24845-24854.
[19] K. Li, A. Niemczyk, K. Świerczek, A. Stępień, Y. Naumovich, J. Dąbrowa, M. Zajusz, K. Zheng, B. Dabrowski, Co-free triple perovskite $La_{1.5}Ba_{1.5}Cu_3O_{7\pm\delta}$ as a promising air electrode material for solid oxide fuel cells, Journal of Power Sources, 532 (2022).
[20] Z. Zhang, D. Xie, J. Ni, C. Ni, $Ba_2YCu_3O_{6+\delta}$-based cathode material for proton-conducting solid oxide fuel cells, Ceramics International, 47 (2021) 14673-14679.
[21] S.A. Sunshine, L.F. Schneemeyer, T. Siegrist, D.C. Douglass, J.V. Waszczak, R.J. Cava, E.M. Gyorgy, D.W. Murphy, Stabilization of strontium analogs of barium yttrium cuprate perovskites via chemical substitution, Chemistry of Materials, 1 (1989) 331-335.
[22] A. Tarancón, M. Burriel, J. Santiso, S.J. Skinner, J.A. Kilner, Advances in layered oxide cathodes for intermediate temperature solid oxide fuel cells, Journal of Materials Chemistry, 20 (2010) 3799-3813.
[23] S. Chen, J. Jin, H. Chen, L. Guo, Performance of $YBa_2Cu_3O_{7-\delta}$-$La_{0.6}Sr_{0.4}Co_{0.2}Fe_{0.8}O_{3-\delta}$ composite cathode for intermediate-temperature solid oxide fuel cells, Journal of Alloys and Compounds, 879 (2021) 160458.
[24] S. Sengodan, S. Choi, A. Jun, T.H. Shin, Y.-W. Ju, H.Y. Jeong, J. Shin, J.T.S. Irvine, G. Kim, Layered oxygen-deficient double perovskite as an efficient and stable anode for direct hydrocarbon solid oxide fuel cells, Nature Materials, 14 (2015) 205-209.
[25] J.G. Fletcher, J.T.S. Irvine, A.R. West, J.A. Labrincha, J.R. Frade, F.M.B. Marques, Polarization behavior of yttrium barium copper oxide electrodes on yttria-stabilized zirconia electrolytes, Materials Research Bulletin, 29 (1994) 1175-1182.
[26] Q. Zhou, T. He, Q. He, Y. Ji, Electrochemical performances of $LaBaCuFeO_{5+x}$ and $LaBaCuCoO_{5+x}$ as potential cathode materials for intermediate-temperature solid oxide fuel cells, Electrochemistry Communications, 11 (2009) 80-83.
[27] Y. Ling, B. Lin, L. Zhao, X. Zhang, J. Yu, R. Peng, G. Meng, X. Liu, Layered perovskite LaBaCuMO5+x (M=Fe, Co) cathodes for intermediate-temperature protonic ceramic membrane fuel cells, Journal of Alloys and Compounds, 493 (2010) 252-255.
[28] C.B. Gopal, S.M. Haile, An electrical conductivity relaxation study of oxygen transport in samarium doped ceria, J. Mater. Chem. A, 2 (2014) 2405-2417.
[29] P. Cayado, D. Hauck, D. Barthlott, M. Erbe, J. Hänisch, B. Holzapfel, Determination of the Oxygen Chain Ordering in $REBa_2Cu_3O_{7-\delta}$ by Electrical Conductivity Relaxation Measurements, ACS Applied Electronic Materials, 3 (2021) 5374-5382.
[30] F. Ciucci, ECRTOOLS, in, 2012.
[31] W. Feng, Y. Song, T. Liu, J. Li, X. Zhang, J. Wang, G. Wang, X. Bao, Orthorhombic $Y_{0.95-x}Sr_xCo_{0.3}Fe_{0.7}O_{3-\delta}$ anode for oxygen evolution reaction in solid oxide electrolysis cells, Fundamental Research, 1 (2021) 439-447.
[32] A.W. Mombrú, H. Pardo, L. Suescun, B.H. Toby, W.A. Ortiz, C.A. Negreira, F.M. Araújo-Moreira, Influence of oxygen disorder on the magnetic properties of $LaBaCuFeO_{5+\delta}$: an EXAFS and neutron diffraction study, Physica C: Superconductivity, 356 (2001) 149-159.
[33] H. Pardo, W.A. Ortiz, F.M. Araújo-Moreira, L. Suescun, B. Toby, E. Quagliata, C.A. Negreira, K. Prassides, A.W. Mombrú, A new structure in the $REBaCuFeO_{5+\delta}$ series: $LaBaCuFeO_{5+\delta}$. Structure and magnetic properties in the $La_{1-x}Pr_xBaCuFeO_{5+\delta}$ system, Physica C: Superconductivity, 313 (1999) 105-114.

[34] L. Er-Rakho, C. Michel, F. Studer, B. Raveau, The oxygen-deficient perovskite $Ba_{0.5}La_{0.5}Fe_{1-x}Cu_xO_{2.75-x/2+\delta}$—A *p*-type semi-conductor with high Cu(III) and fe(IV) contents, Journal of Physics and Chemistry of Solids, 48 (1987) 377-382.
[35] D. Marrocchelli, S.R. Bishop, H.L. Tuller, B. Yildiz, Understanding Chemical Expansion in Non-Stoichiometric Oxides: Ceria and Zirconia Case Studies, Advanced Functional Materials, 22 (2012) 1958-1965.
[36] H. Guo, M.A. Patino, N. Ichikawa, T. Saito, R. Watanabe, M. Goto, M. Yang, D. Kan, Y. Shimakawa, Oxygen Release and Incorporation Behaviors Influenced by A-Site Cation Order/Disorder in $LaCa_2Fe_3O_9$ with Unusually High Valence $Fe^{3.67+}$, Chemistry of Materials, 34 (2022) 345-350.
[37] Y. Zhang, B. Chen, D. Guan, M. Xu, R. Ran, M. Ni, W. Zhou, R. O'Hayre, Z. Shao, Thermal-expansion offset for high-performance fuel cell cathodes, Nature, 591 (2021) 246-251.
[38] D. Chen, F. Wang, H. Shi, R. Ran, Z. Shao, Systematic evaluation of Co-free $LnBaFe_2O_{5+\delta}$ (Ln=Lanthanides or Y) oxides towards the application as cathodes for intermediate-temperature solid oxide fuel cells, Electrochimica Acta, 78 (2012) 466-474.
[39] Z. Zhu, J. Qian, Z. Wang, J. Dang, W. Liu, High-performance anode-supported solid oxide fuel cells based on nickel-based cathode and $Ba(Zr_{0.1}Ce_{0.7}Y_{0.2})O_{3-\delta}$ electrolyte, Journal of Alloys and Compounds, 581 (2013) 832-835.
[40] G. Xiao, Q. Liu, S. Wang, V.G. Komvokis, M.D. Amiridis, A. Heyden, S. Ma, F. Chen, Synthesis and characterization of Mo-doped $SrFeO_{3-\delta}$ as cathode materials for solid oxide fuel cells, Journal of Power Sources, 202 (2012) 63-69.
[41] H.M. O'Bryan, P.K. Gallagher, Expansion of $Pb_2Sr_2Y_{1-x}Ca_xCu_3O_{8+\delta}$ and $Ba_2YCu_3O_{6+\delta}$, MRS Online Proceedings Library, 169 (1989) 1093-1096.
[42] C. Niedrig, S.F. Wagner, W. Menesklou, S. Baumann, E. Ivers-Tiffée, Oxygen equilibration kinetics of mixed-conducting perovskites BSCF, LSCF, and PSCF at 900 °C determined by electrical conductivity relaxation, Solid State Ionics, 283 (2015) 30-37.
[43] N. Li, L. Sun, Q. Li, T. Xia, L. Huo, H. Zhao, Electrode properties of $CuBi_2O_4$ spinel oxide as a new and potential cathode material for solid oxide fuel cells, Journal of Power Sources, 511 (2021).
[44] Z. Gao, L.V. Mogni, E.C. Miller, J.G. Railsback, S.A. Barnett, A perspective on low-temperature solid oxide fuel cells, Energy & Environmental Science, 9 (2016) 1602-1644.
[45] D. Chen, Z. Shao, Surface exchange and bulk diffusion properties of $Ba_{0.5}Sr_{0.5}Co_{0.8}Fe_{0.2}O_{3-\delta}$ mixed conductor, International Journal of Hydrogen Energy, 36 (2011) 6948-6956.
[46] E. Fabbri, L. Bi, D. Pergolesi, E. Traversa, High-performance composite cathodes with tailored mixed conductivity for intermediate temperature solid oxide fuel cells using proton conducting electrolytes, Energy & Environmental Science, 4 (2011).
[47] M. Wegmann, L. Watson, A. Hendry, XPS Analysis of Submicrometer Barium Titanate Powder, J. Am. Ceram. Soc., 87 (2008) 371-377.
[48] A.B. Christie, J. Lee, I. Sutherland, J.M. Walls, An XPS study of ion-induced compositional changes with group II and group IV compounds, Applications of Surface Science, 15 (1983) 224-237.
[49] D. He, W. Ruan, J. Li, J. Ni, C. Ni, Heterogeneity in the Mo doped $La_{0.55}Sr_{0.45}FeO_3$ cathode for direct CO_2 electrolysis, Chemical Engineering Journal, (2021).
[50] F. Aksoy Akgul, G. Akgul, N. Yildirim, H. Unalan, R. Turan, Influence of thermal annealing on microstructural, morphological, optical properties and surface electronic structure of copper oxide thin films, in, 2015.

[51] Y. Liu, D. Wu, S. Peng, Y. Feng, Z. Liu, Enhanced mineralization of dimethyl phthalate by heterogeneous ozonation over nanostructured $(Cu_2O)_{0.5}\cdot CuO\cdot Fe_2O_3$ surfaces: Synergistic effect and radical chain reactions, Separation and Purification Technology, 209 (2018).
[52] D. Shoemaker, J. Li, R. Seshadri, Unraveling Atomic Positions in an Oxide Spinel with Two Jahn-Teller Ions: Local Structure Investigation of $CuMn_2O_4$, Journal of the American Chemical Society, 131 (2009) 11450-11457.
[53] N. Hou, J. Gan, Q. Yan, Y. Zhao, Y. Li, Improved electrochemical oxidation kinetics of $La_{0.5}Ba_{0.5}FeO_{3-\delta}$ anode for solid oxide fuel cells with fluorine doping, Journal of Power Sources, 521 (2022).
[54] B. Li, J.T.S. Irvine, J. Ni, C. Ni, High-performance and durable alcohol-fueled symmetrical solid oxide fuel cell based on ferrite perovskite electrode, Applied Energy, 306 (2022).
[55] B. Li, S. He, J. Li, X. Yue, J.T.S. Irvine, D. Xie, J. Ni, C. Ni, A Ce/Ru Codoped $SrFeO_{3-\delta}$ Perovskite for a Coke-Resistant Anode of a Symmetrical Solid Oxide Fuel Cell, ACS Catalysis, 10 (2020) 14398-14409.
[56] A. Rodriguez José, D.W. Goodman, The Nature of the Metal-Metal Bond in Bimetallic Surfaces, Science, 257 (1992) 897-903.
[57] R. Peng, T. Wu, W. Liu, X. Liu, G. Meng, Cathode processes and materials for solid oxide fuel cells with proton conductors as electrolytes, Journal of Materials Chemistry, 20 (2010) 6218-6225.
[58] R.L. Barns, R.A. Laudise, Stability of superconducting $YBa_2Cu_3O_7$ in the presence of water, 51 (1987) 1373-1375.
[59] T. Hong, K.S. Brinkman, C. Xia, Barium Carbonate Nanoparticles as Synergistic Catalysts for the Oxygen Reduction Reaction on $La_{0.6}Sr_{0.4}Co_{0.2}Fe_{0.8}O_{3-\delta}$ Solid-Oxide Fuel Cell Cathodes, ChemElectroChem, 3 (2016) 805-813.
[60] T. Hong, F. Chen, C. Xia, Barium carbonate nanoparticle as high temperature oxygen reduction catalyst for solid oxide fuel cell, Electrochemistry Communications, 51 (2015) 93-97.